A High-Efficiency and Broadband Folded Reflectarray Based on an Anisotropic Metasurface for Generating Orbital Angular Momentum Vortex Beams

ZHEN-YU YU [ID], YUN-HUA ZHANG, (Member, IEEE), AND HUO-TAO GAO [ID]
School of Electronic Information, Wuhan University, Wuhan 430072, China

Corresponding authors: Yun-Hua Zhang (zhangyunhua@whu.edu.cn) and Huo-Tao Gao (gaoght863@163.com)

ABSTRACT In this paper, a low-profile folded reflectarray (FRA) assembled by an anisotropic metasurface is proposed to generate high-efficiency and broadband orbital angular momentum (OAM) vortex waves in the Ka band. In order to suppress the mutual coupling and increase the polarization conversion efficiency, a dual-polarization phase matching method (DPPMM) for helical wavefront construction is developed to achieve minimum phase compensation error in the orthogonal direction. A compact subwavelength anisotropic meta-atom with orthogonal ‖-shaped structure is designed to achieve flexible wavefront manipulation and high-resolution phase compensation for x and y-polarization incident waves. After the optimization design, nearly 100% cross-polarization conversion efficiency for the anisotropic metasurface can be achieved at the working frequency of 12 GHz. To validate the proposed design method, an OAM FRA with 24×24 meta-atoms is fabricated and measured. The measurement results show that the aperture efficiency of the proposed FRA carried with the OAM mode $l = 1$ is significantly improved and reaches 20.2%. Moreover, the OAM bandwidth and 3-dB gain bandwidth reach 22.5% and 25%, respectively.

INDEX TERMS High efficiency, broadband, orbital angular momentum (OAM), folded reflectarray (FRA), optimization.

I. INTRODUCTION

In 1992, orbital angular momentum (OAM) as one of the essential physical quantities was first observed in the field of light [1]. Unlike the spin angular momentum (SAM) connecting with polarization states to code or encode electromagnetic (EM) waves, OAM has infinite orthogonal fraction and integer modes to potentially increase the channel capacity in theory [2]. Therefore, the OAM can provide a novel freedom degree to achieve high speed and large capacity communication. As an innovative work [3], [4], the OAM was extended to the radio domain by B. Thidé *et al*, who successfully demonstrated the feasibility of increasing the channel capacity for wireless communication.

However, a high-efficiency and broadband vortex beam generator with a low profile still remains one of the main challenges for the OAM system. In order to generate the

OAM vortex beam, a helical phase factor $e^{il\varphi}$ should be introduced for the EM wave, where l is the topological charge and φ is the azimuthal angle. In the early days, the spiral phase plate (SPP) and holographic plate are two primary methods to generate OAM beams by constructing the desired helical phase shift [5]–[8]. However, the remarkable drawbacks of massive volume and the unacceptably high dielectric loss limit their application in the radio domain. The circular antenna array (CAA) as another method has been adapted to generate OAM by exciting the discrete currents based on Nyquist's theory [9]–[12]. Nevertheless, the complex and high-cost phase-shifted network is unavoidable for CAA.

In recent decades, the metasurface, as an advanced version of metamaterial, has made great development and progress [13]–[18]. Metasurface shows a robust ability to flexibly manipulate the phase-amplitude characteristics and polarization states of EM waves. Thus, the high-performance OAM generator based on metasurface has been a research hot spot in recent years [19]–[27]. However, the conventional

OAM reflectarray based on the metasurface has a high profile, which makes it difficult to integrate with other active circuits. An FRA carried with OAM can effectively decrease the full profile by employing the anisotropic metasurface and polarization gate array. Some excellent works have been reported in the field of OAM FRA [28], [29]. In [28], a high polarization separation FRA is proposed to generate vortex beam with OAM mode $l = 1$. However, the size of the proposed meta-atom is larger than half wavelength, which causes difficulty for the anisotropic metasurface to construct the helical wavefront phase with high-resolution, resulting in a low aperture efficiency for this OAM FRA. In [29], an FRA inherently integrated with a planar source is creatively proposed to generate a Bessel beam carried with OAM mode $l = 1$. Nevertheless, the phase manipulation range of the square-shaped meta-atom cannot entirely cover $360°$ and the mutual coupling at the orthogonal direction is neglected for the anisotropic metasurface, which leads to a low-efficiency and narrow gain bandwidth for the proposed OAM FRA.

In this work, an FRA composed of the anisotropic metasurface is proposed and investigated for generating the high-efficiency and broadband OAM beam. In order to weaken the mutual coupling and increase the aperture efficiency, a dual-polarization phase matching method (DPPMM) is developed to optimize the phase distribution of the anisotropic metasurface. A compact anisotropic meta-atom with a small size of $0.4\lambda \times 0.4\lambda$ is employed to achieve accurate and high-resolution phase compensation. Nearly 100% polarization conversion efficiency is achieved at the design frequency of 12 GHz, and the broadband OAM beam with high mode purity is generated from 11 GHz to 13.7 GHz. Compared with [28], [29], both the simulation and measurement results demonstrate that the proposed OAM FRA can generate a more highly efficient vortex beam with a broader bandwidth. This paper is organized as follows. The basic working principle of the proposed OAM FRA is illustrated in section II. The design of the anisotropic meta-atom is presented in section III. The optimization processes and the experimental verification of the OAM FRA are reported in section IV.

II. CONCEPT AND WORKING PRINCIPLE

The FRA, as an evolved version of the reflectarray antenna, features a low profile, high gain, and easy fabrication [30]. In recent years, great development has been witnessed in the field of FRA, and many excellent works have been proposed to meet different requirements [31]–[34]. As a beam convergence device, FRA mainly consists of the primary reflector and secondary reflector. Due to the advantages of feasible phase manipulation, high-efficiency polarization conversion, and low fabrication cost, a planar and ultrathin metasurface can be employed as the main reflector for the FRA. By introducing a polarization gate array as the secondary reflector, the profile of the FRA can be effectively reduced by half compared with the conventional reflectarray.
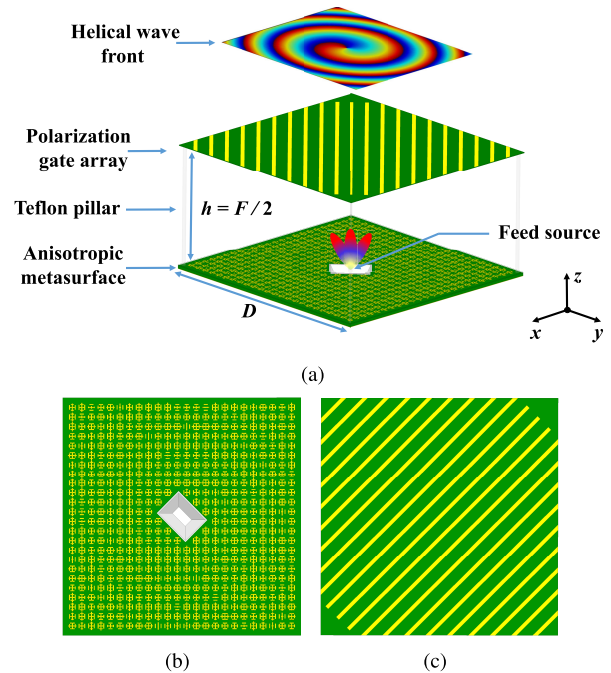
FIGURE 1. Configuration of the proposed OAM FRA. (a) 3-D view. (b) designed anisotropic metasurface. (c) designed polarization gate array.

Therefore, the FRA based on the anisotropic metasurface can be a good candidate to generate high-performance OAM vortex beam.

The configuration of the proposed OAM FRA is presented in Fig. 1. The FRA consists of four main components, including an anisotropic metasurface for phase tuning and polarization conversion, a horn antenna as the feed source, a polarization gate array for the polarization selection, and a Teflon pillar for support and stability. The anisotropic metasurface is composed of subwavelength meta-atoms, and the polarization gate array is realized with printed metallic strips. The detailed working principle of the OAM FRA can be described as follows. The quasi-spherical wave, which polarization is parallel to the long edge of the metallic strip, is emitted by the feed source. Due to the polarization selection characteristic, the incidence wave can be reflected toward the anisotropic metasurface by the polarization gate array. By regulating the dimension of the subwavelength meta-atom appropriately, the polarization of the reflected wave will be twisted $90°$, and the helical phase wavefront will be formed. After the polarization is rotated, the radiated field can pass through the polarization gate array without loss, and the OAM beam can be generated. In addition, the distance between the anisotropic metasurface and the polarization gate array is half of the focal length to cover the radiation power from the feed source.

III. ANISOTROPIC META ATOM DESIGN

For the linear polarization wave incidence, the reflection coefficient of an anisotropic meta-atom can be described by

TABLE 1. Optimized geometry parameters for the proposed anisotropic meta-atom.

parameter	m	n	w	d
value	0.6	0.6	2 mm	1 mm
parameter	h_1	h_2	p	
value	0.5 mm	2 mm	10 mm	

the matrix

$$R_{voh} = \begin{bmatrix} R_{vv} & R_{vh} \\ R_{hv} & R_{hh} \end{bmatrix}$$
$$= \begin{bmatrix} cos\phi & sin\phi \\ -sin\phi & cos\phi \end{bmatrix} \begin{bmatrix} R_{xx} & 0 \\ 0 & R_{yy} \end{bmatrix} \begin{bmatrix} cos\phi & -sin\phi \\ sin\phi & cos\phi \end{bmatrix}$$
(1)

where R_{vv}, R_{hh}, R_{xx} and R_{yy} are the co-polarization reflection coefficients under vertical-polarization, horizontal-polarization, x-polarization and y-polarization normal incidences, R_{vh}, R_{hv}, R_{xy} and R_{yx} are the corresponding cross-polarization reflection coefficients, and ϕ is the angle between the *voh* coordinate and *xoy* coordinate. According to (1), the detailed reflection coefficients at the *voh* coordinate can be written as

$$R_{vv} = R_{xx}cos^2\phi + R_{yy}sin^2\phi \quad (2a)$$
$$R_{vh} = (R_{yy} - R_{xx})cos\phi sin\phi \quad (2b)$$
$$R_{hv} = (R_{yy} - R_{xx})cos\phi sin\phi \quad (2c)$$
$$R_{hh} = R_{xx}sin^2\phi + R_{yy}cos^2\phi \quad (2d)$$

According to the above analysis, the ideal cross-polarization conversion can be achieved, when R_{xx}, R_{yy}, and ϕ satisfy the following conditions

$$R_{xx} = R_{yy}e^{\pm j\pi}, \quad \phi = 45° \quad (3)$$

Besides, the anisotropic meta-atom should possess a sufficient phase range completely covering 360° and have the ability to adjust the reflection phase in the orthogonal direction independently to realize high-efficient polarization conversion and flexible wavefront construction for the metasurface device.

As shown in Fig. 2(a), a subwavelength anisotropic meta-atom is employed to meet the requirements. The meta-atom has a lattice size of $p = 10$ mm, which equals 0.4λ at the working frequency of 12 GHz. Two orthogonal |||-shaped patches are respectively etched on the thickness $h_1 = 0.5$ mm and the thickness $h_2 = 2$ mm F4B substrates with $\varepsilon_r = 2.2$ and $tan\delta = 0.0009$. The dual-layer construction can benefit broadening of the working bandwidth and reduce the mutual coupling in the orthogonal direction for the anisotropic meta-atom [35], [36]. The dimension relation of the middle metallic dipole and the adjacent metallic dipole can be expressed as $a = l_x \times m$ and $b = l_y \times n$, where m and n are the ratio coefficients for the metallic dipole. Fig. 2(b) shows that the incident wave with vertical polarization illuminates the anisotropic meta atom, which can be decomposed to two orthogonal electric field vectors of


(a)

(b)
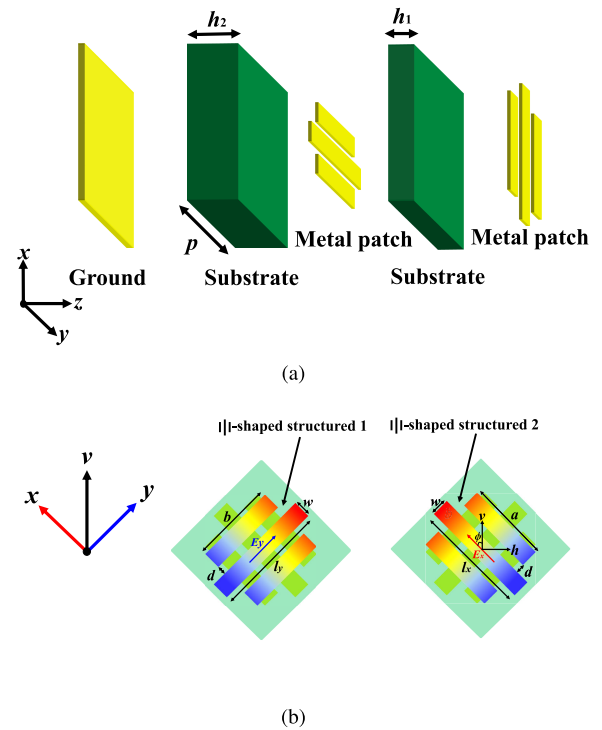
FIGURE 2. Configuration of the proposed anisotropic meta atom. (a) exploded view. (b) top view.

E_x and E_y. Due to the metallic ground excitation, the incident wave can be reflected without any loss for the reflection type anisotropic meta-atom. Hence, the reflection coefficients of R_{xx} and R_{yy} satisfy $|R_{xx}| = |R_{yy}| = 1$ naturally. Then, the perfect cross-polarization conversion efficiency can be achieved when the phase difference in the orthogonal direction satisfies Arg(R_{xx}) - Arg(R_{yy}) $= \pm\pi$ without considering the mutual coupling between the upper and lower |||-shaped patches.

To optimize the electromagnetic performance of the anisotropic meta-atom, the full-wave electromagnetic simulation is performed in numerical software HFSS. According to the above analysis, the 360° phase adjustment range at the orthogonal direction is necessary for the anisotropic meta-atom to achieve precise helical wavefront construction. For the |||-shaped patches, two LC lumped circuits in parallel are constructed. Therefore, phase compensation and polarization conversion can be achieved to properly adjust the length of the upper and lower metal patch. The optimized geometry parameters for the proposed anisotropic meta-atom are displayed in Table 1. After parameter optimization, the reflection phases of the meta atom as a function of frequency and length l_y (or l_x) under TE wave (or TM wave) incidence are shown in Fig. 3(a)-(b). It can be seen that the reflection phase range reaches 360° with the length of l_x (or l_y) changing from 1 mm to 10 mm for TE and TM wave incidence at the working frequency of 12 GHz. Precious helical wavefront construction is expected to be achieved. Besides, a good linear phase as the frequency changes from 11 GHz to 14 GHz is displayed, which is crucially significant to broaden the bandwidth of
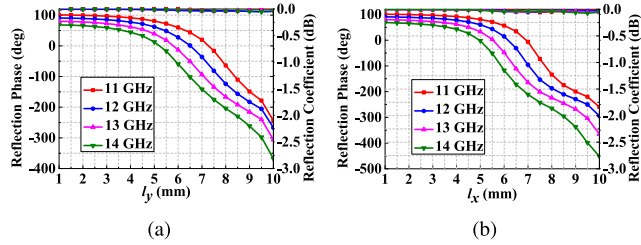
FIGURE 3. Reflection phases and amplitudes of the anisotropic meta-atom as a function of frequency and length of the metallic dipole. (a) TE wave incidence. (b) TM wave incidence.
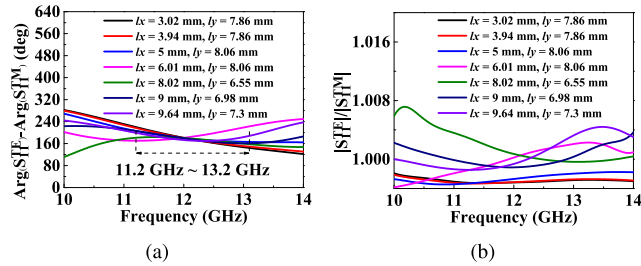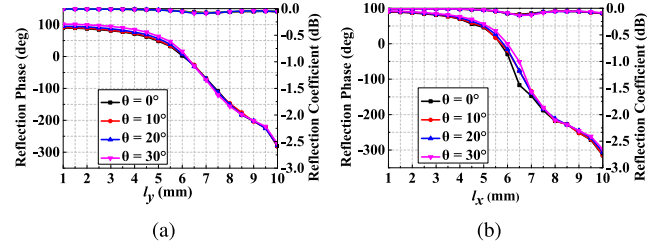

FIGURE 4. Phases difference and the ratio of reflection coefficients under TE and TM wave incidence for different meta-atoms. (a) phase difference. (b) reflection coefficient.

FIGURE 5. Reflection phases and amplitudes versus the length of the metallic dipole l_y (or l_x) under different incident angles. (a) TE wave incidence. (b) TM wave incidence.

FIGURE 6. Working principle of the anisotropic metasurface.

the metasurface. In order to further verify the characteristic of broadband polarization conversion for the proposed meta atom, the phase difference $Arg(S_{11}^{TE}) - Arg(S_{11}^{TM})$ and the ratio of reflection coefficients $|S_{11}^{TE}|/|S_{11}^{TM}|$ under TE and TM wave incidence for different meta-atoms are shown in Fig. 4(a)-(b). It can be seen that the phase difference $Arg(S_{11}^{TE}) - Arg(S_{11}^{TM})$ can remain between $180° \pm 40°$ from 11.2 GHz to 13.2 GHz with different dimensions of meta-atoms. Especially at 12 GHz, $Arg(S_{11}^{TE}) - Arg(S_{11}^{TM})$ remains about $180°$. Meanwhile, $|S_{11}^{TE}|/|S_{11}^{TM}|$ is maintained between 0.996 and 1.008 from 10 GHz to 14 GHz for different meta-atoms. Therefore, high-efficiency and broadband polarization conversion is expected to be achieved. Since most of the meta-atoms are illuminated obliquely by the feed source, it is significant to analyze the sensitivity of the meta-atom under oblique incidence. The reflection phases and amplitudes versus the length of the metallic dipole l_y (or l_x) with different incident angles are shown in Fig. 5(a)-(b). Owing to the good electromagnetic characteristics of the anisotropic meta-atom, the reflection phases change slightly at different incident angles. Therefore, the helical wavefront is constructed under the circumstance of normal incidence.
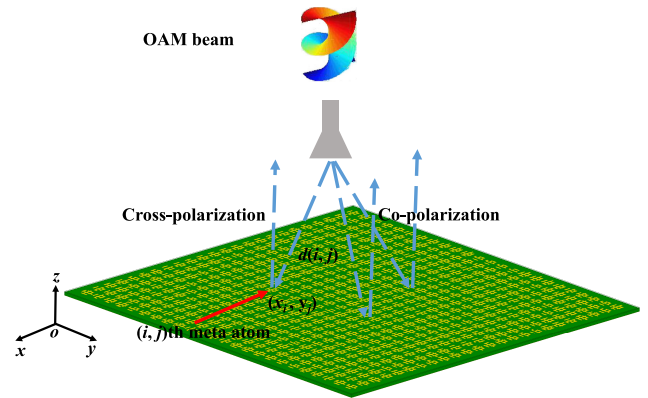
IV. OAM FOLDED REFLECTARRAY ANTENNA DESIGN

A. WAVEFRONT PHASE CONSTRUCTION AND OPTIMIZATION

Due to the good phase manipulation ability of the anisotropic meta-atom, a high-performance anisotropic metasurface can be constructed as the main reflector of the FRA to achieve helical wavefront construction and high-efficiency cross-polarization conversion. The helical phase distribution

of the anisotropic metasurface in the orthogonal direction with $e^{il\varphi}$ can be written as

$$
\begin{cases}
\varphi_x(i,j) = \dfrac{2\pi}{\lambda} \times d(i,j) + l \times \arctan(\dfrac{y_j}{x_i}) \\
\varphi_y(i,j) = \dfrac{2\pi}{\lambda} \times d(i,j) + l \times \arctan(\dfrac{y_j}{x_i}) + \pi
\end{cases} \tag{4}
$$

where λ is the wavelength at the working frequency, $d(i,j)$ is the distance between the phase center of the feed source and meta-atom, and (x_i, y_j) is the central coordinate of the meta-atom. The working principle of the anisotropic metasurface is shown in Fig. 6.

In this article, an anisotropic metasurface with dimension $D = 250$ mm (24×24 meta-atoms) carrying OAM mode $l = 1$ is designed, corresponding to an effective area of $9.6\lambda \times 9.6\lambda$ at the working frequency of 12 GHz. According to Eq. (4), the desired phase compensation for each meta-atom on the aperture surface can be calculated. Ideally, the reflection phases in the orthogonal direction can be adjusted independently for the anisotropic meta-atom. However, there is a strong near-field coupling effect when the meta-atom is at the resonant frequency. When the length of the metallic dipole changes in the x-direction, the reflection phases in the y-direction will be distorted. Similarly, the reflection phases in x-direction will be influenced when the length of the metallic dipole changes at the y-direction. According to Eq. (3), phase compensation error between the desired phase and the achieved phase will reduce the polarization conversion efficiency for the anisotropic
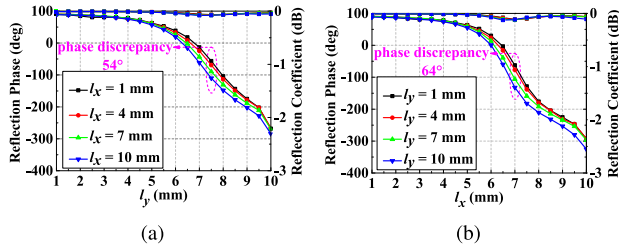
FIGURE 7. Reflection phases and amplitudes versus the length of the metallic dipole l_x (or l_y) with difference values l_y (or l_x) at working frequency 12 GHz. (a) TE wave incidence. (b) TM wave incidence.

metasurface device. However, the mutual coupling of the anisotropic meta-atom is always neglected for OAM wavefront engineering to decrease the efficiency of the metasurface device [19], [20]. To analyze the mutual coupling in the orthogonal direction, the reflection phases of TM wave (or TE wave) incidence versus l_x (or l_y) at 12 GHz for different l_y (or l_x) are calculated, which are displayed in Fig. 7. It can be seen that the maximum phase discrepancy is about 54° by varying l_y from 1 to 10 mm for different l_x, and the maximum phase discrepancy is about 64° by varying l_x from 1 to 10 mm for different l_y. Thus, the reflection phases in the orthogonal direction cannot be adjusted independently for the designed anisotropic meta-atom.

To weaken the mutual coupling and achieve high precision helical wavefront construction, an optimization method called DPPMM is introduced to optimize the phase distribution on the aperture surface of the anisotropic metasurface. The optimization fitness function about the minimum phase compensation error in the orthogonal direction is defined as

$$\Delta\varphi\,(i,j) = |\varphi_x\left(l_x, l_y\right) - \varphi_x\,(i,j)\,| + |\varphi_y\left(l_y, l_x\right) - \varphi_y\,(i,j)\,|$$
$$(5)$$

where $\Delta\varphi\,(i,j)$ is the phase compensation error for each meta-atom, $\varphi_x\left(l_x, l_y\right)$ and $\varphi_y\left(l_y, l_x\right)$ are the achieved phase compensation in the x and y-direction respectively, and $\varphi_x\,(i,j)$ and $\varphi_y\,(i,j)$ are the desired phase compensation in the x and y-direction respectively. To search the minimum $\Delta\varphi\,(i,j)$ for each meta-atom in the anisotropic metasurface, two databases were established based on the reflection phases in Fig. 7. The entire optimization processes for the helical wavefront construction are shown in Fig. 8.

The 24×24 meta-atoms on the aperture surface of the anisotropic metasurface are optimized in the x and y-directions to attain the best dimension of l_x and l_y at the working frequency of 12 GHz. The desired phase compensation in the orthogonal direction is shown in Fig. 9(a)-(b). The entire optimization processes were implemented by an Intel Core i7-8700 CPU costing 824 seconds. The colormap of the achieved minimum phase compensation error is shown in Fig. 10(a). It can be seen that the maximum phase compensation error is about 1.8° on the whole aperture surface of the metasurface. To further demonstrate the achieved high-efficiency polarization conversion, the polarization
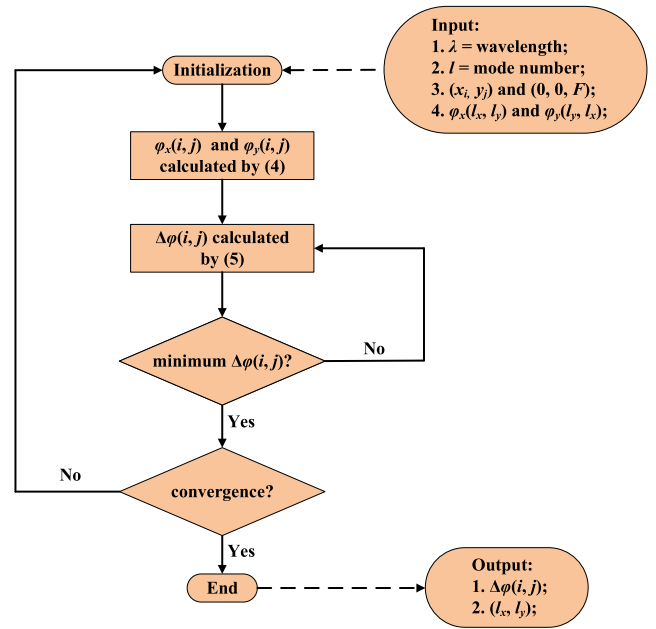
FIGURE 8. Optimization processes for the helical wavefront construction.
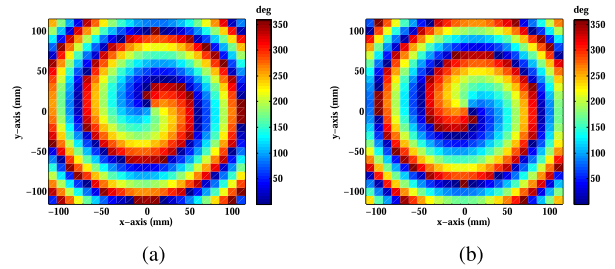
FIGURE 9. Desired phase compensation. (a) desired phase compensation at the *x*-direction. (b) desired phase compensation at the *y*-direction.

conversion efficiency for each meta-atom is calculated. According to [37], the polarization conversion efficiency η can be written as

$$\eta = \frac{2|\left(R_{xx} - R_{yy}\right)/2|^2}{[|R_{xx}|^2 + |R_{xy}|^2 + |R_{yx}|^2 + |R_{yy}|^2]} \qquad (6)$$

where the cross-polarization coefficients $R_{xy} = R_{yx} = 0$. The calculated polarization conversion efficiency for each meta-atom on the aperture surface is shown in Fig. 10(b). It can be observed that the polarization conversion efficiency is higher than 0.99 on the whole aperture surface. The mutual coupling in the orthogonal direction is well suppressed and high-efficiency polarization conversion is achieved at the working frequency of 12 GHz.

B. POLARIZATION GATE ARRAY DESIGN

The polarization gate array is the main component of the FRA, which can be constructed simply by printing metallic strips on a dielectric substrate. The geometry of the polarization gate array is displayed in Fig. 11(a). The polarization gate array has a polarization selective effect for the linear polarization incident wave. The polarization direction of the
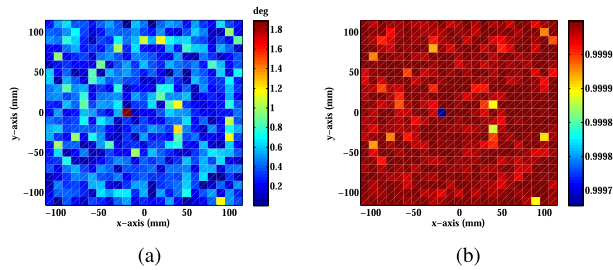
FIGURE 10. Achieved minimum phase compensation error and polarization conversion efficiency on the aperture surface. (a) achieved minimum phase compensation error. (b) polarization conversion efficiency.
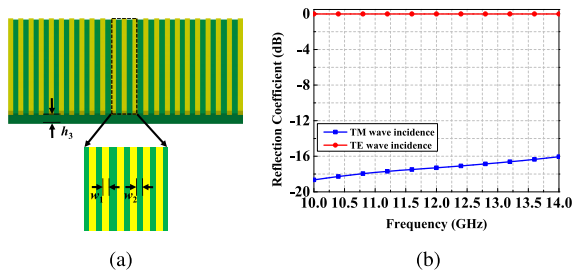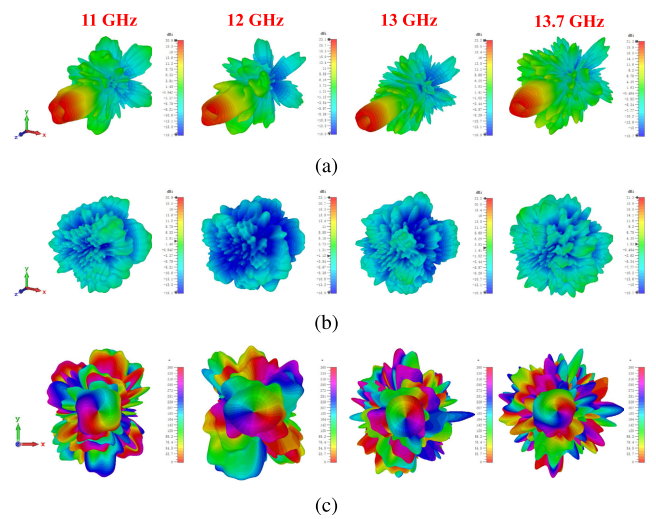

FIGURE 11. (a) Geometry of the polarization gate array. (b) reflection coefficient of the polarization gate array for TE and TM waves incidence.

FIGURE 12. Simulation 3-D radiation patterns at the 11 GHz, 12 GHz, 13 GHz, and 13.7 GHz, respectively. (a) simulation co-pol radiation patterns. (b) simulation cro-pol radiation patterns. (c) simulation phase patterns.

FIGURE 13. Fabricated OAM FRA and the measurement environment. (a) fabricated anisotropic metasurface. (b) fabricated polarization gate array. (c) near-field test. (d) far-field test.

incident wave parallel to the long edge of the metallic strip can be reflected, while the polarization direction of the incident wave vertical to the long edge of the metallic strip can transmit the polarization gate array without loss. The performance of the polarization gate array can be improved by adjusting the width and the gap of the metallic strip. In this design, metallic strips with a width of $w_1 = 2$ mm and a gap of $w_2 = 2$ mm are etched on a thickness $h_3 = 0.508$ mm Arlon DiClad 880 substrate with $\varepsilon_r = 2.2$ and $tan\delta = 0.0009$. The reflection coefficient for orthogonal linear polarization wave incidence is displayed in Fig. 11(b). It can be observed that the reflection coefficients of the polarization gate array are about 0 dB for TE wave incidence, while the reflection coefficients of the polarization gate array are all lower than -15 dB from 10 GHz to 14 GHz for TM wave incidence. Excellent polarization selectivity is excepted to be achieved for the designed polarization gate array.
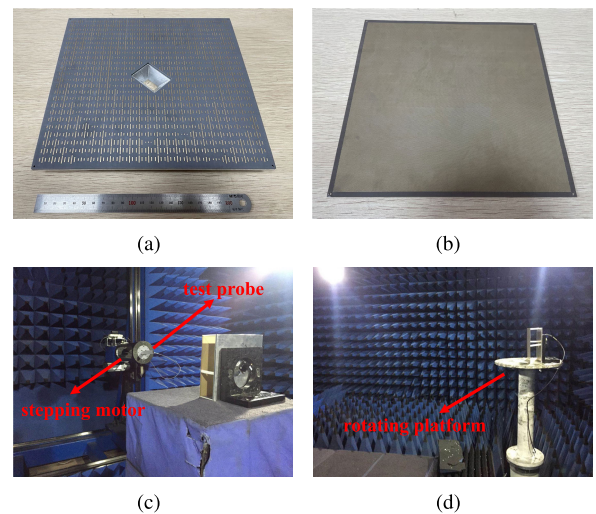
C. SIMULATION AND MEASUREMENT RESULTS

A 250 mm $\times$ 250 mm FRA consisting of an anisotropic metasurface and a polarization gate array is designed to generate mode $l = 1$ vortex beams. Four Teflon pillars are employed to support the metasurface and polarization gate array. A pyramidal horn antenna with WR-75 standard waveguide embedded into the metasurface is employed as the feed source. Compared to the conventional reflectarray, the profile of the OAM FRA can be decreased by a half. The focal length of the OAM FRA can be calculated by

$$F = \frac{D}{4 tan\left(\alpha_{-10\text{dB}}/2\right)} \quad (7)$$

where D is the dimension of the anisotropic metasurface, and $\alpha_{-10\text{dB}}$ is the angle of the -10 dB beamwidth. The focal diameter ratio (F/D) is set as 0.61 in this design.

In order to validate this design, full-wave simulation is implemented by CST MWS Studio for the proposed OAM FRA. The simulated 3-D radiation patterns at 11 GHz, 12 GHz, 13 GHz, and 13.7 GHz are shown in Fig. 12, respectively. As shown in Fig. 12(a), the co-polarization (co-pol) radiation patterns all presented amplitude vacuum at the center from 11 GHz to 13.7 GHz, which is consistent with the characteristics of vortex beam. Moreover, the simulation radiation gains are higher than 20.9 dBi in the operating frequency band. Fig. 12(b) presents the cross-polarization (cro-pol) radiation patterns. Due to the
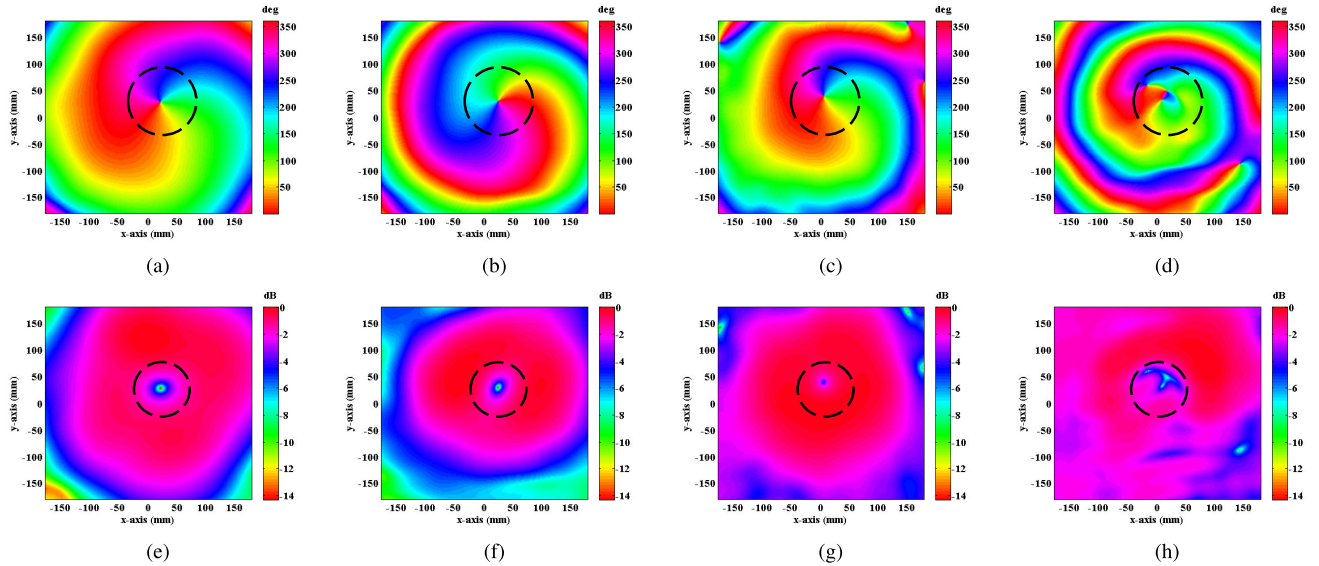
FIGURE 14. Near-field measurement phases and amplitudes at the 11 GHz, 12 GHz, 13 GHz, and 13.7 GHz, respectively. (a)-(d) measurement phases. (e)-(h) measurement amplitudes.

good polarization selectivity of the polarization gate array, the cro-pol gains are all lower than 2.6 dBi across the wide-band. The characteristic of high polarization purity is displayed for the proposed OAM FRA. According to the phase patterns in Fig. 12(c), the anti-clockwise helical phase distribution varying from 0° to 360° can be observed clearly in the entire band, which corresponds to the characteristics of mode $l = 1$ vortex wave and demonstrate the correctness of our design.

To further verify the design in the experiment, the proposed OAM FRA is fabricated and measured. The anisotropic metasurface and polarization gate array are manufactured by PCB technology. The feed source is rotated $\phi = 45°$ around the z-axis so that the incident electric field is uniformly distributed in the orthogonal direction. The measurement is carried out in an anechoic chamber to avoid outside interference for the near-field and far-field tests. The fabricated OAM FRA and measurement environment are shown in Fig. 13. Plane scanning is performed to measure the near-field phases and amplitudes. In this experiment, the area of the scanning plane is 360 mm × 360 mm, and a test probe is employed to measure the electric field with a step of 10 mm controlled by a stepping motor. The distance between the antenna under test and the probe is 700 mm. Due to the high polarization purity of the proposed OAM FRA, the phases and amplitudes of the electric field in the x-direction are measured. The measured near-field phases and amplitudes distribution from 11 GHz to 13.7 GHz are presented in Fig. 14. It can be observed that a clear helical phase distribution varying from 0° to 360° can be observed from 11 GHz to 13.7 GHz, which is consistent with the simulation phase patterns. Meanwhile, a typical circular distribution with zero amplitude at the center is exhibited in the entire measurement frequency range, which corresponds to the amplitude vacuum characteristics of the simulated 3-D

radiation pattern. With the measurement frequency increasing, the measurement phases deteriorate gradually. The main reasons for this phenomenon are manufacturing tolerance and phase compensation error increase at high frequency. Besides, the mode purity of the reflection vortex wave with different OAM modes is analyzed at the measurement frequencies by using the Discrete Fourier Transform (DFT) algorithm. According to [38], the mode purity can be calculated by

$$P(\alpha) = \frac{1}{2\pi} \int_0^{2\pi} \psi(\varphi) \, d\varphi \, e^{-jl\varphi} \tag{8}$$

$$\psi(\varphi) = \sum_{-\infty}^{+\infty} P(\alpha) \, e^{-jl\varphi} \tag{9}$$

where $\psi(\varphi)$ is the discrete phase values around the circumstance of the z-axis. The calculated mode purity for the measurement phases distribution considering mode $l = -3$ to 3 at 11 GHz, 12 GHz, 13 GHz, and 13.7 GHz are shown in Fig. 15. It shows that the mode purity of topological charge $l = 1$ reaches 96.7% at 12 GHz for the measurement phase distribution. The high mode purity with mode $l = 1$ is achieved at the working frequency of 12 GHz. Moreover, the mode purity of topological charge $l = 1$ reaches 85.4%, 77.5%, and 79.8% at 11 GHz, 13 GHz, and 13.7 GHz, respectively for the proposed OAM FRA. It demonstrates that the broadband OAM wave with high mode purity is generated.

The far-field performance is measured on a rotating platform for the proposed OAM FRA, which is presented in Fig. 13(d). The measured and simulated radiation patterns at 11 GHz, 12 GHz, 13 GHz, and 13.7 GHz are displayed in Fig. 16(a)-(d). It can be seen that the measured radiation patterns have good agreement with the simulated ones in the entire frequency band. The measurement radiation patterns

TABLE 2. Comparisons between the proposed OAM FRA and the previous work.

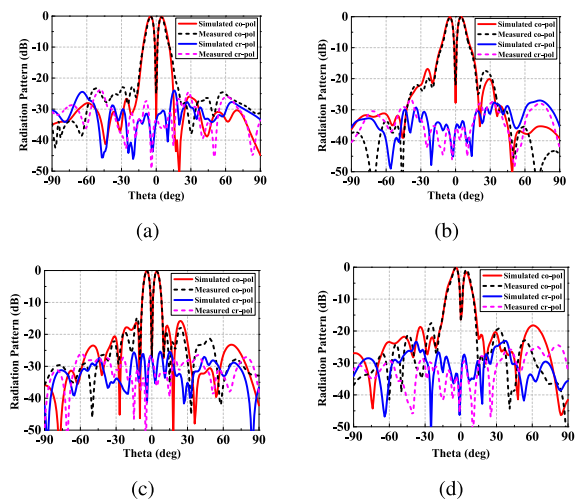| Ref.	Type	f_0 (GHz)	Size	Profile	Meta-atom size	Meta-atom phase range	Mode	Gain (dBi)	Peak efficiency	Gain bandwidth	OAM bandwidth
[19]	RA	15	$10.5\lambda_0$	High	$0.4\lambda_0$	272°	$l=1$	21	11.6%	NA	13%
[20]	RA	10	$10.5\lambda_0$	High	$0.5\lambda_0$	400°	$l=1$	19.9	7.2%	20% (1-dB)	20%
[21]	RA	5.8	$3.87\lambda_0$	$4.94\lambda_0$	$0.38\lambda_0$	377°	$l=1$	15.4	22.6%	NA	NA
[22]	TA	5.14	$4.91\lambda_0$	NA	$0.31\lambda_0$	360°	$l=1$	NA	NA	NA	9.7%
[28]	FRA	32	$10.88\lambda_0$	$3.3\lambda_0$	$0.64\lambda_0$	400°	$l=1$	21.5	12.09%	Narrow	Narrow
[29]	FRA	40.25	$12.48\lambda_0$	$3.1\lambda_0$	$0.4\lambda_0$	320°	$l=1$	NA	NA	Narrow	Narrow
This work	**FRA**	**12**	**$9.6\lambda_0$**	**$2.9\lambda_0$**	**$0.4\lambda_0$**	**360°**	$l=1$	**23.5**	**20.2%**	**25% (3-dB)**	**22.5%**

NA: not available, RA: reflectarray, TA: transmitarray
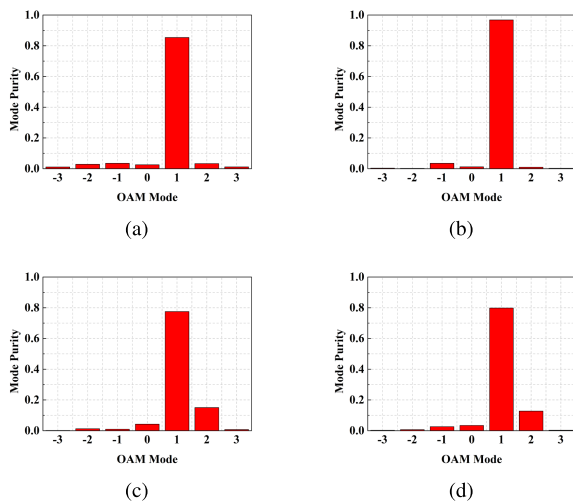
FIGURE 15. Calculated mode purity of the OAM FRA for the measurement phases distribution. (a) 11 GHz. (b) 12 GHz. (c) 13 GHz. (d) 13.7 GHz.

FIGURE 16. Simulation and measurement radiation patterns at (a) 11 GHz, (b) 12 GHz, (c) 13 GHz and (d) 13.7 GHz.
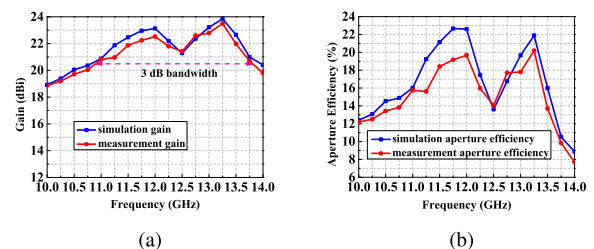
FIGURE 17. Gain and aperture efficiency vary with the frequency. (a) simulated and measured gain. (b) simulated and measured aperture efficiency.

show good conical beams, and the cone-angles are about $\theta = \pm 5°$. This corresponds to the characteristics of the mode $l = 1$ vortex wave. The measured sidelobe levels (SLLs) are all lower than -16 dB from 11 GHz to 13.7 GHz. Compared with the simulation results, the measured SLLs are slightly increased. Meanwhile, the high polarization purity in the broadband is presented, which is in line with our expectations. The measurement cro-pol levels are all lower than -20 dB in the broadside direction. Fig. 17(a)-(b) shows that the radiation gain and aperture efficiency vary with the frequency of the proposed OAM FRA. It can be observed that the maximum simulation and measurement gains reach 23.9 dBi and 23.5 dBi, respectively. Moreover, the simulation and measurement aperture efficiencies reach 21.9% and 20.2%. The main reasons causing the measured radiation performance deterioration is manufacture and alignment errors for the designed OAM FRA. Moreover, the proposed OAM FRA has 25% measurement 3-dB gain bandwidth from 10.8 GHz to 13.8 GHz. High efficiency and broadband characteristics are presented for the proposed OAM antenna.

To further demonstrate the advantage of our work, a comparison between some reported OAM generators and the proposed OAM FRA is shown in Table 2. It can be seen that

our work has a lower profile and higher aperture efficiency with the same OAM mode $l = 1$ than the conventional OAM reflectarray [19], [20]. Compared with [21], the full profile of our work is effectively reduced and a broader OAM bandwidth is presented. Compared with the transmission OAM metasurface in [22], our work has a broader OAM bandwidth and lower cost. Moreover, the proposed OAM antenna has a higher aperture efficiency and broader bandwidth compared with the same type of FRA [28], [29]. In summary, high aperture efficiency and good bandwidth characteristics are presented for the proposed OAM FRA.

V. CONCLUSION

We developed a novel low profile FRA based on an anisotropic metasurface to generate high-efficiency and broadband vortex beams. Aiming to weaken mutual coupling in the orthogonal direction, a DPPMM is proposed to obtain the optimal dimension of each subwavelength meta-atom. After optimization, a perfect polarization conversion efficiency is achieved at the working frequency. Both the near-field and far-field experimental results demonstrate good performance of the proposed OAM generator. The measurement results show that the aperture efficiency of the proposed antenna is remarkably improved compared with existing OAM FRAs. Moreover, the measurement OAM bandwidth and 3-dB gain bandwidth reach 22.5% and 25%, respectively. Besides, the proposed design method can be developed to generate arbitrary integer and fractional OAM modes. Due to the excellent performance of the proposed OAM FRA, it is promising in various applications in the future.

REFERENCES

[1] L. Allen, M. W. Beijersbergen, R. J. C. Spreeuw, and J. P. Woerdman, "Orbital angular momentum of light and the transformation of Laguerre–Gaussian laser modes," *Phys. Rev. A, Gen. Phys.*, vol. 45, no. 11, p. 8185, Jun. 1992.

[2] A. E. Willner, H. Huang, Y. Yan, Y. Ren, N. Ahmed, G. Xie, C. Bao, L. Li, Y. Cao, Z. Zhao, and J. Wang, "Optical communications using orbital angular momentum beams," *Adv. Opt. Photon.*, vol. 7, pp. 66–106, Mar. 2015.

[3] B. Thidé, H. Then, J. Sjöholm, K. Palmer, J. Bergman, T. D. Carozzi, Y. N. Istomin, N. H. Ibragimov, and R. Khamitova, "Utilization of photon orbital angular momentum in the low-frequency radio domain," *Phys. Rev. Lett.*, vol. 99, no. 8, Aug. 2007, Art. no. 087701.

[4] F. Tamburini, E. Mari, A. Sponselli, B. Thidé, A. Bianchini, and F. Romanato, "Encoding many channels on the same frequency through radio vorticity: First experimental test," *New J. Phys.*, vol. 14, no. 3, Mar. 2012, Art. no. 033001.

[5] E. Brasselet, M. Malinauskas, A. Žukauskas, and S. Juodkazis, "Photopolymerized microscopic vortex beam generators: Precise delivery of optical orbital angular momentum," *Appl. Phys. Lett.*, vol. 97, no. 21, Nov. 2010, Art. no. 211108.

[6] Q. Wang, X. Sun, and P. Shum, "Generating doughnut-shaped beams with large charge numbers by use of liquid-crystal spiral phase plates," *Appl. Opt.*, vol. 43, no. 11, pp. 2292–2297, 2004.

[7] X. Hui, S. Zheng, Y. Hu, C. Xu, X. Jin, H. Chi, and X. Zhang, "Ultralow reflectivity spiral phase plate for generation of millimeter-wave OAM beam," *IEEE Antennas Wireless Propag. Lett.*, vol. 14, pp. 966–969, 2015.

[8] E. Karimi, B. Piccirillo, E. Nagali, L. Marrucci, and E. Santamato, "Efficient generation and sorting of orbital angular momentum eigenmodes of light by thermally tuned q-plates," *Appl. Phys. Lett.*, vol. 94, no. 23, 2009, Art. no. 231124.

[9] B. Liu, Y. Cui, and R. Li, "A broadband dual-polarized dual-OAM-mode antenna array for OAM communication," *IEEE Antennas Wireless Propag. Lett.*, vol. 16, pp. 744–747, 2017.

[10] Z. Zhang, S. Xiao, Y. Li, and B.-Z. Wang, "A circularly polarized multimode patch antenna for the generation of multiple orbital angular momentum modes," *IEEE Antennas Wireless Propag. Lett.*, vol. 16, pp. 521–524, 2017.

[11] H. Li, L. Kang, F. Wei, Y.-M. Cai, and Y.-Z. Yin, "A low-profile dual-polarized microstrip antenna array for dual-mode OAM applications," *IEEE Antennas Wireless Propag. Lett.*, vol. 16, pp. 3022–3025, 2017.

[12] Z. Yang, J. Zhou, L. Kang, B. Liu, G. Yang, and X. Shi, "A closed-loop cross-dipole antenna array for wideband OAM communication," *IEEE Antennas Wireless Propag. Lett.*, vol. 19, no. 12, pp. 2492–2496, Dec. 2020.

[13] J. B. Pendry, "A chiral route to negative refraction," *Science*, vol. 306, no. 5700, pp. 1353–1355, Nov. 2004.

[14] D. Schurig, J. J. Mock, B. J. Justice, S. A. Cummer, J. B. Pendry, A. F. Starr, and D. R. Smith, "Metamaterial electromagnetic cloak at microwave frequencies," *Science*, vol. 314, no. 5801, pp. 977–980, Nov. 2006.

[15] N. Yu, P. Genevet, M. A. Kats, F. Aieta, J.-P. Tetienne, F. Capasso, and Z. Gaburro, "Light propagation with phase discontinuities: Generalized laws of reflection and refraction," *Science*, vol. 334, no. 6054, pp. 333–337, Oct. 2011.

[16] Y. Yuan, K. Zhang, B. Ratni, Q. Song, X. Ding, Q. Wu, S. N. Burokur, and P. Genevet, "Independent phase modulation for quadruplex polarization channels enabled by chirality-assisted geometric-phase metasurfaces," *Nature Commun.*, vol. 11, no. 1, pp. 1–9, Dec. 2020.

[17] M. R. Akram, M. Q. Mehmood, X. Bai, R. Jin, M. Premaratne, and W. Zhu, "High efficiency ultrathin transmissive metasurfaces," *Adv. Opt. Mater.*, vol. 7, no. 11, Jun. 2019, Art. no. 1801628.

[18] M. R. Akram, G. Ding, K. Chen, Y. Feng, and W. Zhu, "Ultrathin single layer metasurfaces with ultra-wideband operation for both transmission and reflection," *Adv. Mater.*, vol. 32, no. 12, Mar. 2020, Art. no. 1907308.

[19] J. Yang, C. Zhang, H. F. Ma, J. Zhao, J. Y. Dai, W. Yuan, L. X. Yang, Q. Cheng, and T. J. Cui, "Generation of radio vortex beams with designable polarization using anisotropic frequency selective surface," *Appl. Phys. Lett.*, vol. 112, no. 20, May 2018, Art. no. 203501.

[20] G.-T. Chen, Y.-C. Jiao, and G. Zhao, "A reflectarray for generating wideband circularly polarized orbital angular momentum vortex wave," *IEEE Antennas Wireless Propag. Lett.*, vol. 18, no. 1, pp. 182–186, Jan. 2019.

[21] H.-F. Huang and S.-N. Li, "High-efficiency planar reflectarray with small-size for OAM generation at microwave range," *IEEE Antennas Wireless Propag. Lett.*, vol. 18, no. 3, pp. 432–436, Mar. 2019.

[22] H. Shi, L. Wang, M. Zhao, J. Chen, A. Zhang, and Z. Xu, "Transparent metasurface for generating microwave vortex beams with cross-polarization conversion," *Materials*, vol. 11, no. 12, p. 2448, Dec. 2018.

[23] H.-F. Huang and S.-N. Li, "Single-layer dual-frequency unit for multifunction OAM reflectarray applications at the microwave range," *Opt. Lett.*, vol. 45, no. 18, pp. 5165–5168, Sep. 2020.

[24] Z. Wang, X. Pan, F. Yang, S. Xu, M. Li, and D. Su, "Design, analysis, and experiment on high-performance orbital angular momentum beam based on 1-bit programmable metasurface," *IEEE Access*, vol. 9, pp. 18585–18596, 2021.

[25] K. Zhang, Y. Yuan, X. Ding, H. Li, B. Ratni, Q. Wu, J. Liu, S. N. Burokur, and J. Tan, "Polarization-engineered noninterleaved metasurface for integer and fractional orbital angular momentum multiplexing," *Laser Photon. Rev.*, vol. 15, no. 1, Jan. 2021, Art. no. 2000351.

[26] J. Yi, M. Guo, R. Feng, B. Ratni, L. Zhu, D. H. Werner, and S. N. Burokur, "Design and validation of an all-dielectric metamaterial medium for collimating orbital-angular-momentum vortex waves at microwave frequencies," *Phys. Rev. A, Gen. Phys.*, vol. 12, no. 3, Sep. 2019, Art. no. 034060.

[27] Y. Meng, J. Yi, S. N. Burokur, L. Kang, H. Zhang, and D. H. Werner, "Phase-modulation based transmitarray convergence lens for vortex wave carrying orbital angular momentum," *Opt. Exp.*, vol. 26, no. 17, pp. 22019–22029, Aug. 2018.

[28] X. Y. Lei and Y. J. Cheng, "High-efficiency and high-polarization separation reflectarray element for OAM-folded antenna application," *IEEE Antennas Wireless Propag. Lett.*, vol. 16, pp. 1357–1360, 2017.

[29] Y. Shen, J. Yang, H. Meng, W. Dou, and S. Hu, "Generating millimeter-wave Bessel beam with orbital angular momentum using reflective-type metasurface inherently integrated with source," *Appl. Phys. Lett.*, vol. 112, no. 14, Apr. 2018, Art. no. 141901.

[30] D. Pilz and W. Menzel, "Folded reflectarray antenna," *Electron. Lett.*, vol. 34, no. 9, pp. 832–833, Apr. 1998.

[31] S. Bildik, S. Dieter, C. Fritzsch, W. Menzel, and R. Jakoby, "Reconfigurable folded reflectarray antenna based upon liquid crystal technology," *IEEE Trans. Antennas Propag.*, vol. 63, no. 1, pp. 122–132, Jan. 2015.

[32] C. Zhang, Y. Wang, F. Zhu, G. Wei, J. Li, C. Wu, S. Gao, and H. Liu, "A planar integrated folded reflectarray antenna with circular polarization," *IEEE Trans. Antennas Propag.*, vol. 65, no. 1, pp. 385–390, Jan. 2017.

[33] Z.-W. Miao, Z.-C. Hao, Y. Wang, B.-B. Jin, J.-B. Wu, and W. Hong, "A 400-GHz high-gain quartz-based single layered folded reflectarray antenna for terahertz applications," *IEEE Trans. THz Sci. Technol.*, vol. 9, no. 1, pp. 78–88, Jan. 2019.

[34] A. Freni, A. Mazzinghi, and G. Carluccio, "Folded reflectarray with spherical polarizer," *IEEE Trans. Antennas Propag.*, vol. 68, no. 5, pp. 3613–3624, May 2020.

[35] J. A. Encinar, "Design of two-layer printed reflectarrays using patches of variable size," *IEEE Trans. Antennas Propag.*, vol. 49, no. 10, pp. 1403–1410, Oct. 2001.

[36] G.-B. Wu, S.-W. Qu, S. Yang, and C. H. Chan, "Broadband, single-layer dual circularly polarized reflectarrays with linearly polarized feed," *IEEE Trans. Antennas Propag.*, vol. 64, no. 10, pp. 4235–4241, Oct. 2016.

[37] H.-X. Xu, H. Liu, X. Ling, Y. Sun, and F. Yuan, "Broadband vortex beam generation using multimode Pancharatnam–Berry metasurface," *IEEE Trans. Antennas Propag.*, vol. 65, no. 12, pp. 7378–7382, Dec. 2017.

[38] E. Yao, S. Franke-Arnold, J. Courtial, S. Barnett, and M. Padgett, "Fourier relationship between angular position and optical orbital angular momentum," *Opt. Exp.*, vol. 14, no. 20, pp. 9071–9076, Oct. 2006.
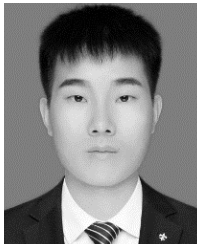
ZHEN-YU YU was born in Hubei, China, in 1991. He received the M.S. degree from Xidian University, Xi'an, China, in 2018. He is currently pursuing the Ph.D. degree with the School of Electronic Information, Wuhan University, Wuhan, China. His research interests include reflectarray antennas, metasurfaces and their applications, and finite difference time domain method.
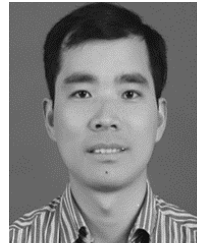
YUN-HUA ZHANG (Member, IEEE) was born in Hubei, China, in 1981. He received the B.S. and M.S. degrees in electronic engineering from Wuhan University, Wuhan, China, in 2003 and 2006, respectively, and the Ph.D. degree in electronic engineering from the University of Leeds, Leeds, U.K., in 2011. From 2010 to 2012, he worked as a Postdoctoral Researcher with Queen's University Belfast, Belfast, U.K. After that, he joined Wuhan University as an Associate Professor. His research interests include antennas, metamaterials and their applications, and computational electromagnetism.

HUO-TAO GAO received the Ph.D. degree in radio physics and the M.S. degree in electromagnetic field and microwave technology from Wuhan University, Wuhan, China. He is currently a Professor with the Electronic Information School, Wuhan University. He has authored or coauthored over 90 articles, and holds seven Chinese patents. His current research interests include the antenna theory and design, art and science of optical rectifying-antennas, radiowave propagation and scattering, radar detection, and signal processing.

• • •